Article

Synthesis of Fe_2O_3/Mn_2O_3 Nanocomposites and Impregnated Porous Silicates for Dye Removal: Insights into Treatment Mechanisms

Soyoung Baek [1], Yasaman Ghaffari [1,2] and Jiyeol Bae [1,2,*]

[1]   Department of Environment Research, Korea Institute of Civil Engineering and Building Technology (KICT), Goyang 10223, Korea
[2]   Department of Environmental Research, University of Science and Technology (UST), Daejeon 34000, Korea
*   Correspondence: baejiyeol@kict.re.kr

Abstract: Fe_2O_3/Mn_2O_3 nanocomposites and impregnated porous silicates ($Fe_2O_3/Mn_2O_3@SiO_2$ [FMS]) were prepared and investigated as catalytic adsorbents. The catalysts were applied for cationic and anionic dye pollutants in the adsorption, Fenton reaction, and photocatalysis processes at a pH of 7. Fe_2O_3/Mn_2O_3 nanoparticles (FM-NPs) were prepared using the co-precipitation method and were impregnated in SiO_2 by the sol–gel process. The synthesized materials were characterized using various sophisticated techniques. Results indicated that the impregnation of bi-metallic NPs in SiO_2 increased the surface area, and the function of the adsorbent also improved. FMS showed a significant adsorption effect, with 79.2% rhodamine B removal within 15 min. Fenton and photocatalyst reaction showed removal rates of 85.3% and 97.9%, respectively, indicating that negatively charged porous silicate attracts cationic pollutants. In the case of the anionic pollutant, Congo red, the adsorption reaction of FMS did not occur, and the removal rate of the photocatalyst reaction was 79%, indicating the repulsive force between the negatively charged silica and the anionic dye. Simultaneously, bi-metal-bonded FM-NPs facilitated the photocatalytic reaction, reducing the recombination of electron-hole pairs. This study provides new insights into the synthesis of FM-NPs and FMS as photocatalytic adsorbents and their photocatalytic mechanisms based on reaction conditions and contaminant characteristics. The developed materials have potential applications for environmental mitigation.

Keywords: dye removal; environmental mitigation; Fenton reaction; nanocomposites; photocatalysis; porous silicates

1. Introduction

With rapid industrial development, the magnitude of production of environmentally hazardous pollutants has increased. Various physical and chemical techniques, such as coagulation, adsorption, and chemical oxidation, are widely used to degrade contaminants from wastewater [1]. However, the demand for advanced treatment methods is urgent owing to the complex nature of generated pollutants [2]. Recently, advanced oxidation processes (AOPs) and oxidation methods based on highly reactive species, such as hydroxyl radicals, have been effectively used for the degradation of diverse toxic compounds in water, including oxidants (H_2O_2 and ozone), energy sources (UV light, ultrasonic, and heat), and catalysts (titanium dioxide, zinc oxide, and Fenton reagent) [3–6]. Among the AOPs, nanoparticle-assisted photocatalytic degradation is an effective removal method that occurs in the presence of reactive species [7–9].

Fe-based catalysts are mostly utilized for wastewater treatment in heterogeneous photocatalysis due to their highly oxidizing properties, low cost, and low environmental toxicity [10]. However, the main drawbacks of using iron as a photocatalyst are sludge formation and narrow pH range [11]. To avoid this problem, bimetallic catalysts, including Cu,

Mn, and Co as supports for Fe, have been explored for the synthesis of heterogeneous Fenton catalysts [7,12]. When catalysts are combined, their properties create a synergistic effect, which enhances the catalytic reaction and compensates for the limitations of iron [13,14]. Thus, recent studies have reported that bimetallic composites can reduce the dosage of hydrogen peroxide, produce more reactive oxygen species, and promote Fe^{3+}/Fe^{2+} redox reactions [15]. Our previous study synthesized an Fe_2O_3/Mn_2O_3 photocatalyst, which could remove 97% of organic dyes within 75 s at neutral pH [7]. Previous literature highlighted the role of bimetallic nanoparticles (NPs) to improve catalytic performance. For instance, MnO_2-Fe_3O_4/CuO hybrid catalysts enhance the decolorization reaction of the dye because of their increased nanoparticle surface area and uniform pore-size compared with Fe_3O_4/CuO [14]. Another study synthesized an $MnO_2/Fe_3O_4/$diatomite nanocomposite and showed almost 100% methylene blue (MB) degradation in 45 min at pH 4–8 [16].

The application of these materials as photocatalysts and adsorbents is being explored because they cooperatively enhance the efficient degradation of organic pollutants from water [17]. Thus, there are many approaches for an advanced catalyst to enhance catalytic activity for environmental and economic benefit [6,18]. Efficient adsorption on the material surface is an important process for achieving photocatalytic efficiency [19]. However, photocatalytic degradation cannot occur in the absence of adsorption [17]. In this regard, many studies have applied photocatalytic adsorbents, such as carbon materials, mesoporous silicon, and metal–organic frameworks, to promote adsorption capacity for pollutant removal [20–22]. With the introduction of a mesoporous SiO_2 support, the photocatalyst may improve the dispersion of NPs, enhancing adsorption on the high surface area of SiO_2 [23]. A previous study indicated that coupling semiconductor materials with mesoporous SiO_2 induces more active sites at the interface, which is favorable for photocatalysis [7,24]. Recent studies have reported that the SiO_2 structure provides sites for the dispersion of NPs and increase in surface area [25].

Many studies have reported the performances of photocatalytic adsorbents [17,19,22]. However, only a few studies have investigated the multi-functional photocatalyst by imparting high porosity adsorbents to the photocatalytic material. Thus, the degradation performance and mechanisms of synthesized photocatalyst were studied on both cationic and anionic molecules. In this context, with the development of bimetallic nanocomposites that are impregnated with porous silicate, their multifunctional performances on both cationic and anionic dye molecules were observed in aqueous solutions. This study aimed to (1) develop bi-metal nanocomposites and porous materials impregnated with these nanocomposites, (2) apply the developed photocatalytic material for the degradation of cationic and anionic organic pollutants in water, and (3) study the pollutant degradation mechanism of these synthesized materials. New Fe_2O_3/Mn_2O_3 and $Fe_2O_3/Mn_2O_3@SiO_2$ (FMS) composites were synthesized. The structure and surface physicochemical characterization of the synthesized materials were analyzed by field-emission scanning electron microscopy (FESEM), high-resolution transmission electron microscopy (HRTEM) with energy dispersive spectroscopy (EDS), X-ray diffraction (XRD) analysis, and Fourier-transform infrared spectroscopy (FTIR). The synthesized photocatalytic adsorbents were applied to remove toxic organic dye pollutants in water under various processing conditions.

2. Results and Discussion

2.1. Characterization of Adsorbents

2.1.1. Scanning Electron Microscopy Energy Dispersive Spectroscopy (SEM-EDS) and High-Resolution Transmission Electron Microscopy Energy Dispersive Spectroscopy (HRTEM-EDS)

Morphologies and components of the synthesized photocatalytic adsorbents were observed using FE-SEM and HRTEM-EDS (Figure 1). Figure 1a shows the synthesized FM-NPs and FMS. FM-NPs have a crystalline coral-like shape, which can be ascribed to the role of cetyltrimethylammonium bromide (CTAB) in the synthesis. EDS mapping confirmed the presence of Fe, Mn, and O. SEM and HRTEM images of FMS (Figure 1b,c) show highly aggregated spherical shapes, which is the general amorphous morphology of

SiO$_2$ [26,27]. SEM-EDS verified the existence of constituent elements (Si, Fe, Mn, and O) on the synthesized photocatalyst surface. Thus, HRTEM-EDS (Figure 1c) characterized Si, O, Fe, and Mn elements of FMS, and these components were present independently on the surface of SiO$_2$ and overlapped with each other. It is well known that unsupported metal oxide nanoparticles aggregate owing to the nanosized particles and surface charge.
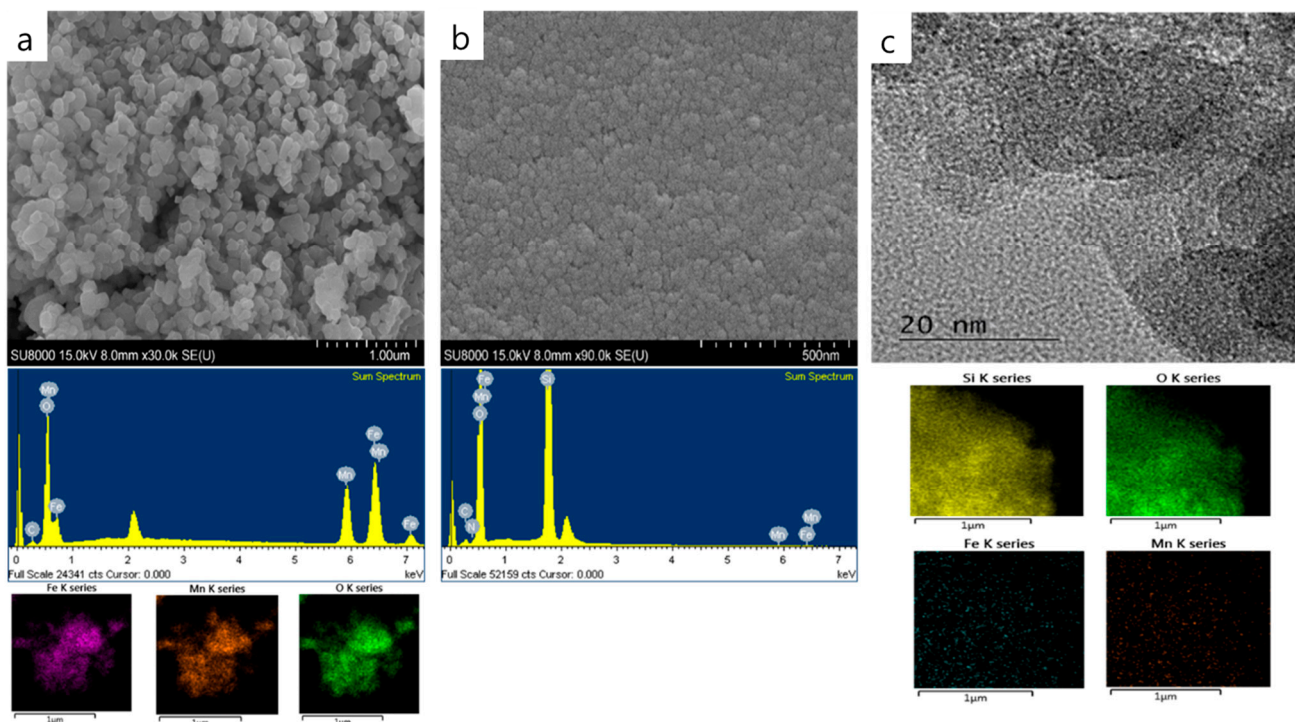

Figure 1. Images for (**a**) SEM-EDS of Fe$_2$O$_3$/Mn$_2$O$_3$ nanoparticles (FM-NPs), (**b**) SEM-EDS of Fe$_2$O$_3$/Mn$_2$O$_3$@SiO$_2$ (FMS), and (**c**) HRTEM-EDS of FMS.

2.1.2. N$_2$ Adsorption–Desorption Isotherm

BET specific surface area of porous materials on the synthesized FM-NPs and FMS were analyzed using N$_2$ adsorption–desorption isotherms (Figure 2, Table 1). The N$_2$ isotherm of the FM-NPs indicated a hysteresis loop for type III nonporous materials, and the estimated surface area was 15.5 m^2/g. The N$_2$ isotherm of FMS was of type IV, which is typical for mesoporous materials. FMS shows an H2 type hysteresis loop, exhibiting complex pore structures. The FMS hysteresis loop shows a similar shape to that of SiO$_2$ silica, suggesting that it has very similar pore characteristics to that of SiO$_2$. The surface area FM-NPs on SiO$_2$ increased marginally from 427.0 m^2/g to 562.4 m^2/g.
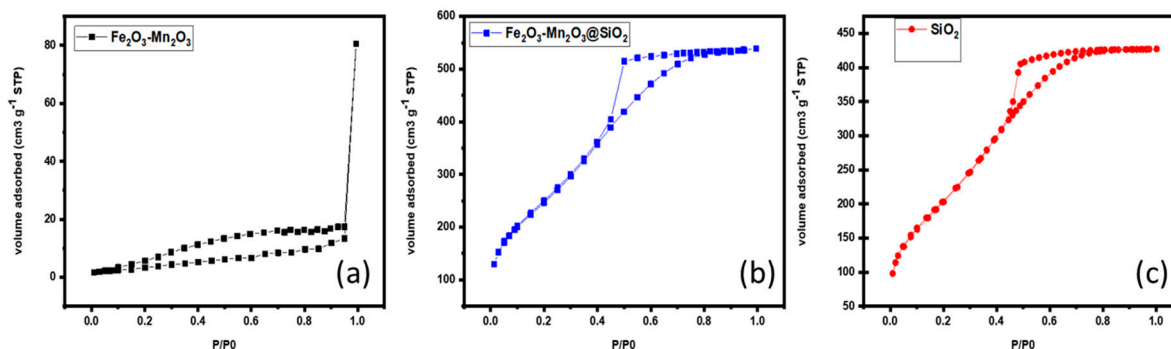

Figure 2. N$_2$ adsorption–desorption isotherm of synthesized (**a**) Fe$_2$O$_3$/Mn$_2$O$_3$ nanoparticles (FM−NPs), and (**b**) Fe$_2$O$_3$/Mn$_2$O$_3$@SiO$_2$ (FMS), and (**c**) bare SiO$_2$.

Table 1. Surface area and porosity properties of synthesized materials.

	BET Surface Area (m^2/g)	Pore Volume $(cm^3 \cdot g^{-1})$	Pore Diameter (nm)
Fe_2O_3/Mn_2O_3 (FM-NPs)	15.6	0.12	3.4
$Fe_2O_3/Mn_2O_3@SiO_2$ (FMS)	562.4	0.54	3.8
SiO_2	427.0	0.56	3.0

2.1.3. X-ray Diffraction (XRD) Analysis

High-resolution X-ray diffraction (XRD) was used to determine the composition and phase structure of the synthesized materials. The diffraction profiles of the materials are shown in Figure 3. The XRD pattern of the FM-NPs matched the peaks of rhombohedral α-Fe_2O_3 (JCPDS #33-0664) and cubic α-Mn_2O_3 (JCPDS #24-0508) [7]. Peakless spectra for bare SiO_2 and FMS exhibit a broad diffraction peak centered at approximately 22.6°, which is assigned to amorphous SiO_2. The diffraction peaks observed in the XRD patterns of FM-NPs were not detected in the FMS, indicating that the FM-NPs were incorporated into the SiO_2. This suggests that the FM-NPs were successfully synthesized in the SiO_2 structure, with low Fe and Mn contents in the nanocomposites.
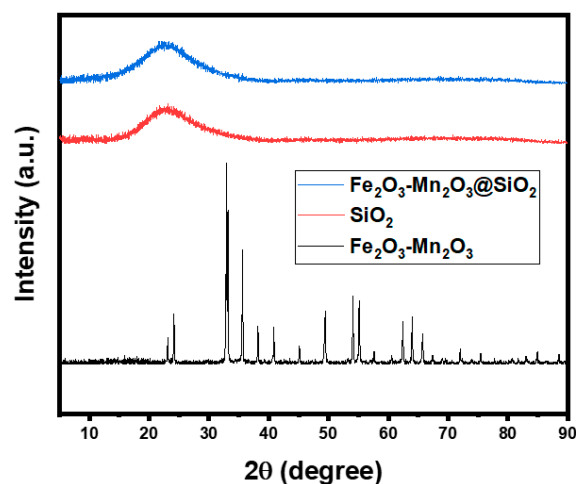

Figure 3. X-ray diffraction (XRD) patterns of synthesized photocatalyst; Fe_2O_3/Mn_2O_3 nanoparticles (FM-NPs), $Fe_2O_3/Mn_2O_3@SiO_2$ (FMS), and bare SiO_2.

ESR spectrum of photocatalyst was recorded at 298 K (Figure 4). The ESR spectrum is a superposition of two signals: one broad signal with a Lorentzian line shape and one well-defined sextet. The high-intensity signal at g = 1.98 was attributed to Fe^{3+} ions in the Fe_2O_3 nanoparticles [28]. The sextet observed was the six-line hyperfine splitting characteristic of Mn^{2+} ions with a nuclear spin I = 5/2 ($-5/2 \leq m \leq +5/2$, $\Delta m = 0$; $m(a)$ = +5/2, $m(f)$ = $-5/2$) [29]. The absence of peaks corresponding to MnO_x and FeO_x in the XRD pattern could be due to the limitation of the XRD sensitivity. However, the ESR results confirmed that in the synthesized photocatalyst, MnO_x and FeO_x existed with Mn^{2+} and Fe^{3+} state, respectively, in the silica matrix.
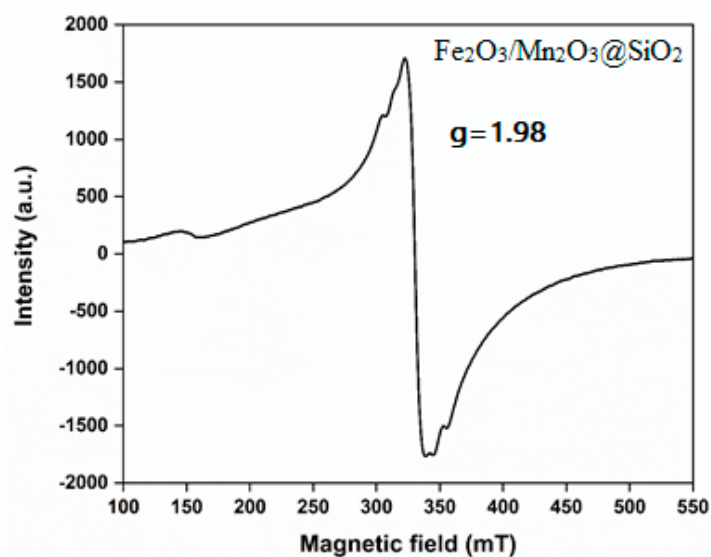
Figure 4. ESR spectrum of synthesized photocatalyst $Fe_2O_3/Mn_2O_3@SiO_2$ (FMS).

2.1.4. Fourier Transform Infrared (FTIR) Spectroscopy

FTIR spectra of the FM-NPs, SiO_2, and FMS are shown in Figure 5. In all the curves in Figure 5, the band at approximately 1635 cm^{-1} can be allocated to the H-O-H stretching and the adsorbed water at 3420 cm^{-1}. For FM-NPs, metal oxide bonds were assigned at 473 cm^{-1} for Mn-O of Mn_2O_3 and 541 cm^{-1} for Fe-O of Fe_2O_3 bonds which is MO4 tetrahedron and MO6 octahedron each. In the FTIR spectrum of SiO_2 and FMS, the absorption bands were assigned to Si-O-Si at 1074 cm^{-1}, 806 cm^{-1}, and Si-O at 461 cm^{-1} [30,31]. The presence of abundant OH groups and H_2O on the surfaces of FMS can play a key role in bonding metal ions from the suspended colloid. In the sol–gel process of FMS, homogeneously distributed Fe^{2+} and Mn^{2+} are absorbed on to the surfaces of spherical silica particles by physical and chemical interactions. Therefore, it is not difficult to find any alterations between bare SiO_2 and FMS because the peak density of the fine FM-NPs is negligible due to its low concentration compared to SiO_2.
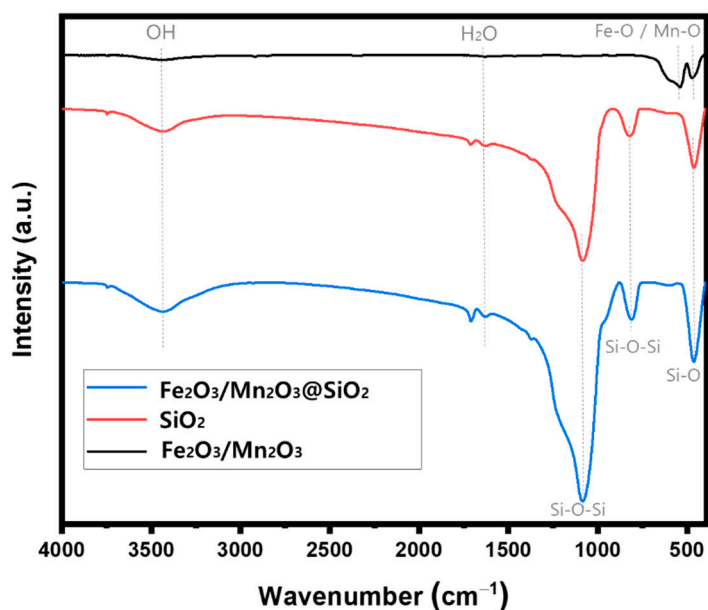

Figure 5. Fourier transform infrared (FTIR) spectra of synthesized photocatalyst; Fe_2O_3/Mn_2O_3 nanoparticles (FM-NPs), $Fe_2O_3/Mn_2O_3@SiO_2$ (FMS), and bare SiO_2.

2.1.5. X-ray Photoelectron Spectroscopy (XPS)

The elemental oxidation of FMS surface was analyzed using X-ray photoelectron spectroscopy (XPS). High energy scans of the full spectrum of elements, O 1s spectrum, Fe 2p spectrum, and Mn 2p spectrum are shown in Figure 6. The O 1s spectrum using Gaussian–Lorentzian distribution shows four different bound state of O, which correspond to the Metal-O at 531.45 eV, Si-O-Si bond at 532.42 eV, O-H at 533.51 eV, and H_2O on the material surface at 534.7 eV (Figure 6b). The formation of Fe_2O_3 and Mn_2O_3 can be confirmed in Figure 6c,d [32]. The spectra of the Fe of FMS were deconvoluted into Fe $2p_{3/2}$ peak at 711.02 eV, and Fe $2p_{1/2}$ peak at 724.98 eV respectively along with two satellite peaks at 718.31 and 732.05 eV. The Fe 2p peak of Fe_2O_3 has been investigated by many researchers, indicating values of between 710.6 and 711.2 eV [33,34]. The satellite peak of Fe_2O_3 is located about 8 eV higher than the Fe $2p_{3/2}$ peak, while Fe_3O_4 does not have a satellite peak. Similar, Mn peaks show Mn $2p_{3/2}$ peak at 641.48 eV and Mn $2p_{1/2}$ peak at 653.34 eV, respectively, implying the spin energy separation of 11.86 eV, which is a demonstration of Mn^{3+} in Mn_2O_3 oxidation state [35].
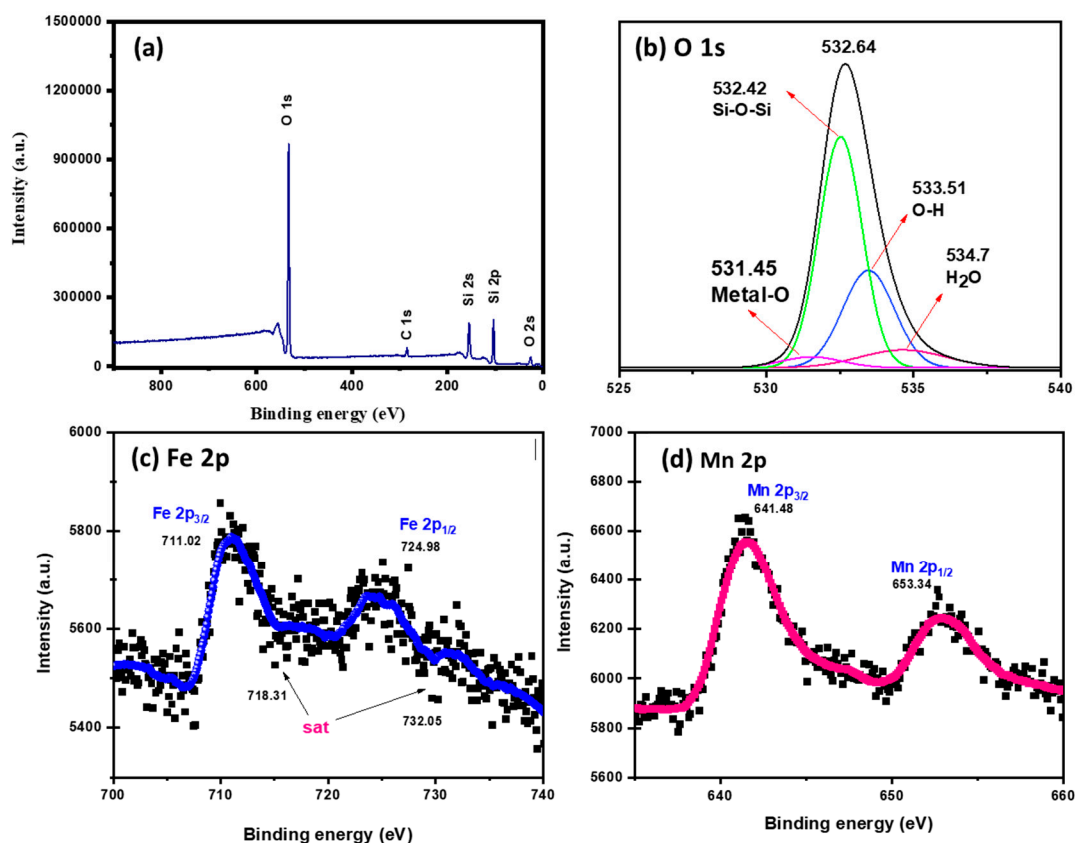

Figure 6. XPS of $Fe_2O_3/Mn_2O_3@SiO_2$ (FMS); (**a**) full spectrum of elements, (**b**) O 1s spectrum, (**c**) Fe 2p spectrum, and (**d**) Mn 2p spectrum.

2.2. Removal of Dyes of Fe_2O_3/Mn_2O_3 Nanoparticles and $Fe_2O_3/Mn_2O_3@SiO_2$

2.2.1. Degradation Performance for Cationic Dye

RhB, a basic cationic dye, was chosen as a model compound to assess the photocatalytic performance of the synthesized materials. The absorption peak of RhB using UV–Vis spectrophotometry was at 558 nm and it was used to measure the degradation rate (C/C_0) of the reaction performance. Figure 7 shows the degradation of RhB by the FM-NPs and FMS under different reaction conditions. The adsorption experiment was first conducted in the dark with FM-NPs and FMS at an initial pH of 7. Figure 6a shows the degradation of RhB via the adsorption reaction, indicating that the positively charged RhB adsorbs on to the surface of synthesized FMS, showing 84.2% degradation due to the charge interaction.

However, the RhB degradation for FM-NPs is up to 35.8% at 120 min, which is much lower than that of FMS (84.2%). This indicates that FM-NPs display negligible adsorption removal, given that the removal rate at 60 min was 6.3%. The inactivity of FM-NPs is due to the lack of a negatively charged surface of materials causing binding between them and the anionic or neutral dye [36]. Another study synthesized different types of Fe-metal oxide nanoparticles for dye degradation. Fe-MnO$_X$ showed the elevated reactivity for dye degradation because of the hindrance in electron-hole pair recombination compared to other Fe bi-metals [36]. As shown in the BET results, FMS exhibits significant adsorption efficiency compared to FM-NPs, which may be attributed to its larger surface area and pore structure. Thus, sufficient surface exposure of O atoms from SiO$_2$ enables strong adsorption on positively charged dyes, according to the XPS results shown above [37].
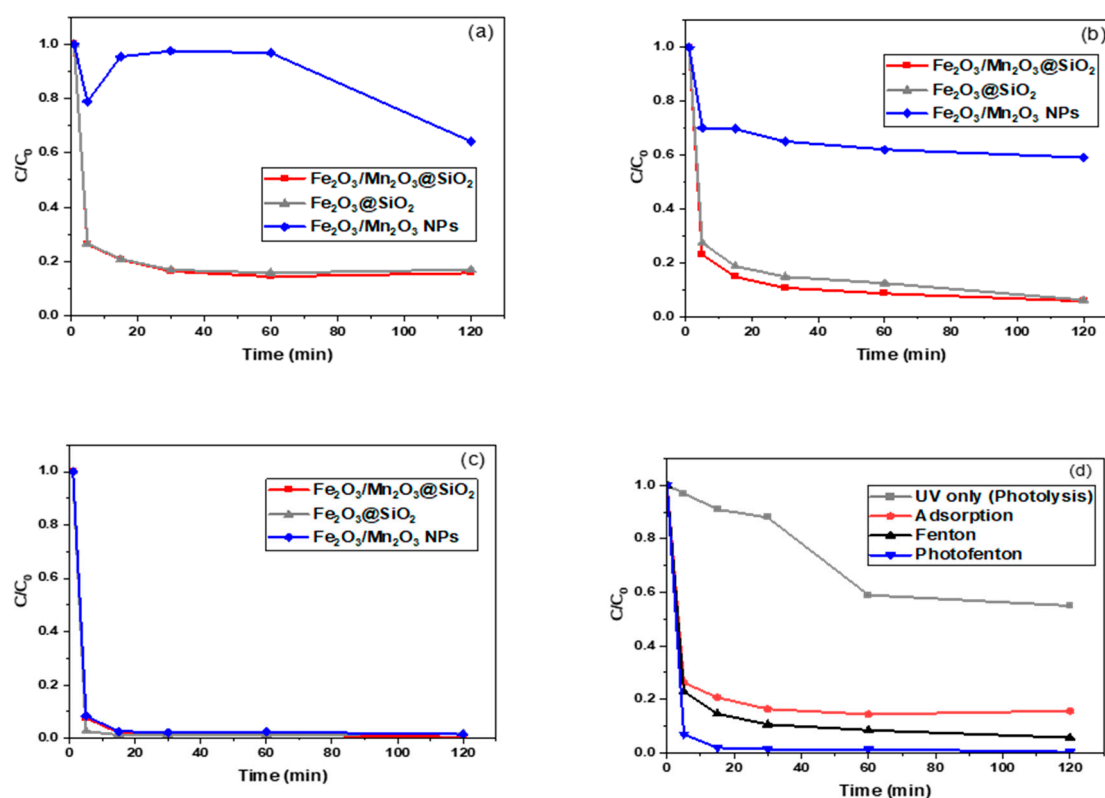

Figure 7. Degradation of rhodamine B (RhB) with Fe$_2$O$_3$/Mn$_2$O$_3$ nanoparticles (FM-NPs), Fe$_2$O$_3$/Mn$_2$O$_3$@SiO$_2$ (FMS) under different conditions; (**a**) Only adsorption (without UV + H$_2$O$_2$), (**b**) Fenton reaction with H$_2$O$_2$ (without UV), (**c**) Photo-Fenton reaction with UV + H$_2$O$_2$ (reaction conditions: catalyst dose = 1 g/L, initial concentration of RhB = 10 mg/L, initial pH = 7), and (**d**) comparison of degradation performance with FMS under different reaction conditions.

In the following Fenton reaction (Figure 7b), the addition of H$_2$O$_2$ improved the degradation efficiency of both FM-NPs and FMS over RhB. The FMS exhibited a significant increase in the removal rate from 6.3% to 40.3% in 60 min, which was mainly ascribed to the generation of radicals. The Fenton reaction reports the generation of hydroxide (OH$^-$) and hydroxyl radicals by the response between iron (Fe^{2+}) and H$_2$O$_2$ [38]. Additionally, the FMS showed a better RhB removal performance as it increased from 84.2% to 92.6% of degradation efficiency, which is attributed to its large surface area and abundant active sites on both FM-NPs. In the presence of H$_2$O$_2$, the subsequent catalytic performance of metal oxide NPs can induce a synergistic catalyst combination because a bi-metal (Fe$_2$O$_3$/Mn$_2$O$_3$) can induce slower electron-hole recombination than a single metal [39,40]. To investigate the subsequent catalytic reaction of Fe^{2+} and Mn^{2+} on FM-NPs, the same Fenton reaction experiment was conducted with the synthesized Fe$_2$O$_3$@SiO$_2$ material

(Figure 7b). Compared to $Fe_2O_3@SiO_2$, FMS had a better degradation efficiency, proving that the Fe_2O_3/Mn_2O_3 pair is a synergistic catalyst for the Fenton reaction.

The photocatalytic performance was examined in the presence of UV light and H_2O_2, and the results are shown in Figure 7c. For the photocatalytic reaction, the FM-NPs and FMS showed excellent removal rate of almost 100% in 15 min. In addition to the adsorption and Fenton reactions, the enhanced photocatalytic performance was highly influential in the degradation of RhB. For the photocatalytic reduction of dye molecules, pH, UV light intensity, and H_2O_2 concentration are critical. The zeta potential of the catalyst was analyzed to investigate the point of zero charge value of FMS. As shown in Figure 8, the point of zero charge of FMS was pH 6, and it had a negative charge at pH 7, which is an experimental condition. In our previous study, we synthesized Mn_2O_3-$Fe_2O_3@SiO_2$ nanocomposites with the addition of urea as a fuel and tested the effect of the zeta potential on UV intensity and H_2O_2 concentration [7]. The zero-point charge of the synthesized materials was at pH 6, which means that the surface of the material was negatively charged at pH 7. Li et al. conducted a catalytic reaction over $MnO_2/Fe_4O_4/$diatomite NPs by varying the pH of the RhB solution ranging from 4 to 8, and the results showed that the removal rates of the dyes under different pH state were almost the same. These results suggest that negatively charged materials can attract organic molecules (RhB), which are cationic dyes They also showed that dye degradation increased with an addition in UV light intensity in the range of 8–32 W, and the excessive H_2O_2 decreased the organic oxidation process owing to the self-quenching of the OH radical [16]. The overdosed H_2O_2 is catalyzed to produce more hydroxyl radicals and increase the collision of free radicals to inhibit its decomposition. SiO_2 adsorbents covered by FM-NPs, which enhance the catalytic function, have chains of a silica hydrogel network (Si-O-Si). This hydrophilic property can hold a large number of O^- sites and induce strong van der Waals interactions with the dye surface [41].
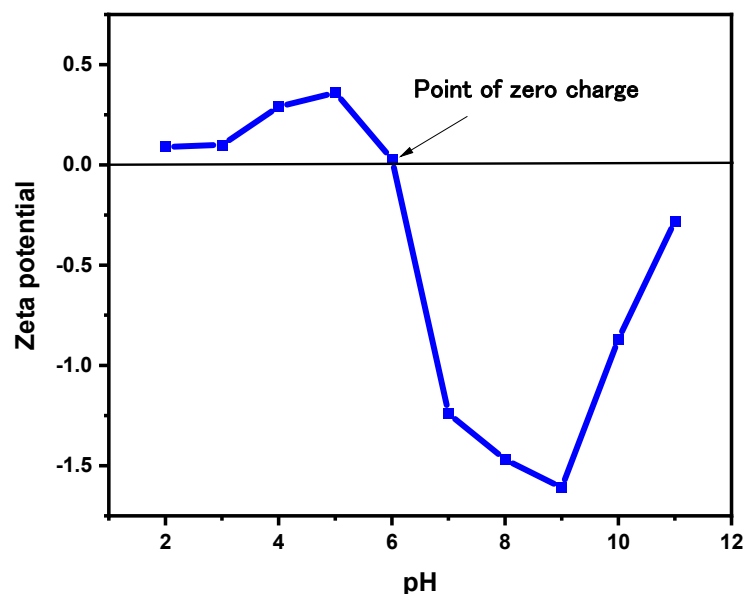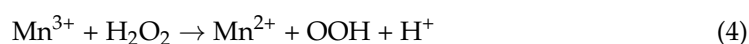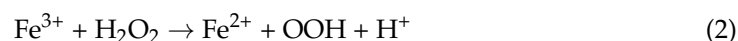

Figure 8. The zeta potential of $Fe_2O_3/Mn_2O_3@SiO_2$ (FMS) in different pH conditions.

The degradation performance of RhB dye of a synthesized photocatalyst adsorbent, FMS, was evaluated and compared under different reaction conditions. Figure 7d shows the degradation of RhB using four methods: UV (photolysis), adsorption, Fenton, and photo-Fenton. FMS (100 mg) was added to 100 mL of RhB solution at a concentration of 10 ppm over a 2 h reaction time to evaluate its performance under different conditions. Figure 7d clearly shows adsorption indicating the impact of FMS on the removal of RhB, resulting in 84.2% removal of the RhB aqueous solution. Interestingly, photolysis (UV

only) showed 42% removal of dye by photons. In photolysis, the H_2O cleaved by UV light generate hydroxyl radicals and interact with target molecule of dye [42]. Fenton and photo-Fenton reactions degraded 94.2% and 99.5% of RhB dye molecules within 60 min, respectively. Interestingly, the RhB dye was quickly removed by adsorption in the first 5 min, and the addition of H_2O_2 (Fenton) enhanced the degradation of the dye. Thus, in the photo-Fenton reaction with added UV, in addition to the Fenton reaction, the degradation of RhB dye was even higher because the Fe_2O_3/Mn_2O_3 nanocomposite in the FMS acts as an effective catalyst under H_2O_2 and UV light (Equations (1)–(4)):

$$Fe^{2+} + H_2O_2 \rightarrow Fe^{3+} + OH + OH^- \tag{1}$$

$$Fe^{3+} + H_2O_2 \rightarrow Fe^{2+} + OOH + H^+ \tag{2}$$

$$Mn^{2+} + H_2O_2 \rightarrow Mn^{3+} + OH + OH^- \tag{3}$$

$$Mn^{3+} + H_2O_2 \rightarrow Mn^{2+} + OOH + H^+ \tag{4}$$

2.2.2. Degradation Performance for Anionic Dye

To compare the degradation capacity of the synthesized photocatalytic adsorbents according to their pollutant properties, Congo red (CR), a benzidine-based anionic, was selected as a model dye molecule. Figure 9 shows CR degradation by FM-NPs and FMS under different reaction conditions. First, dye adsorption with the synthesized material under no UV shows that CR molecules can be marginally adsorbed on to the surface of FMS with Fe^{2+} and Mn^{2+} contents. In contrast, the adsorbents with SiO_2 as the platform showed no adsorption effect (Figure 9a). There is a strong repulsive force between the negatively charged CR and the SiO_2 surface, which supports the ability of SiO_2 in the FMS to strongly adsorb positively charged contaminants (Figure 9b). In the Fenton reaction, which appears when H_2O_2 is injected into the reaction, it can be seen that the catalytic reaction of FM-NPs increased significantly from 12% to 66%. The silica-based material containing metal oxide nanoparticles showed a similar low efficiency in the H_2O_2 reaction, suggesting the presence of an electrostatic attraction reaction between silica and contaminants, which serves as a platform and acts as an important mechanism for reducing pollutants [43]. In the photocatalytic reaction in Figure 9c, a high removal rate (C/C_0) was achieved by FM-NPs and FMS, i.e., almost 100% removal in 15 min. However, the photocatalytic performances of FMS and $Fe_2O_3@SiO_2$ showed an unstable degradation reaction over 120 min, which is attributed to the continuous generation of repulsive forces between the negatively charged silica and anionic dye. In contrast, the photocatalyst, particularly in the case of bi-metal-bonded NPs, indicated that the photocatalytic effect was more stable than in the case of single Fe NPs. This result supports the synergistic effect of the bi-metal discussed above. The degradation performance of the synthesized photocatalyst, FM-NPs, for CR dye was evaluated and compared under different reaction conditions (Figure 9d). UV light had a decomposition effect, which was improved by increasing the reaction time. However, the reaction efficiency and time were lower than those of the Fenton oxidation or photocatalytic reaction. In the case of anionic dye decomposition, FM-NPs did not have a significant adsorption effect on a low specific surface area. However, the effect of the catalyst was significant, and oxidation of the contaminant was ensured in the presence of a UV source.
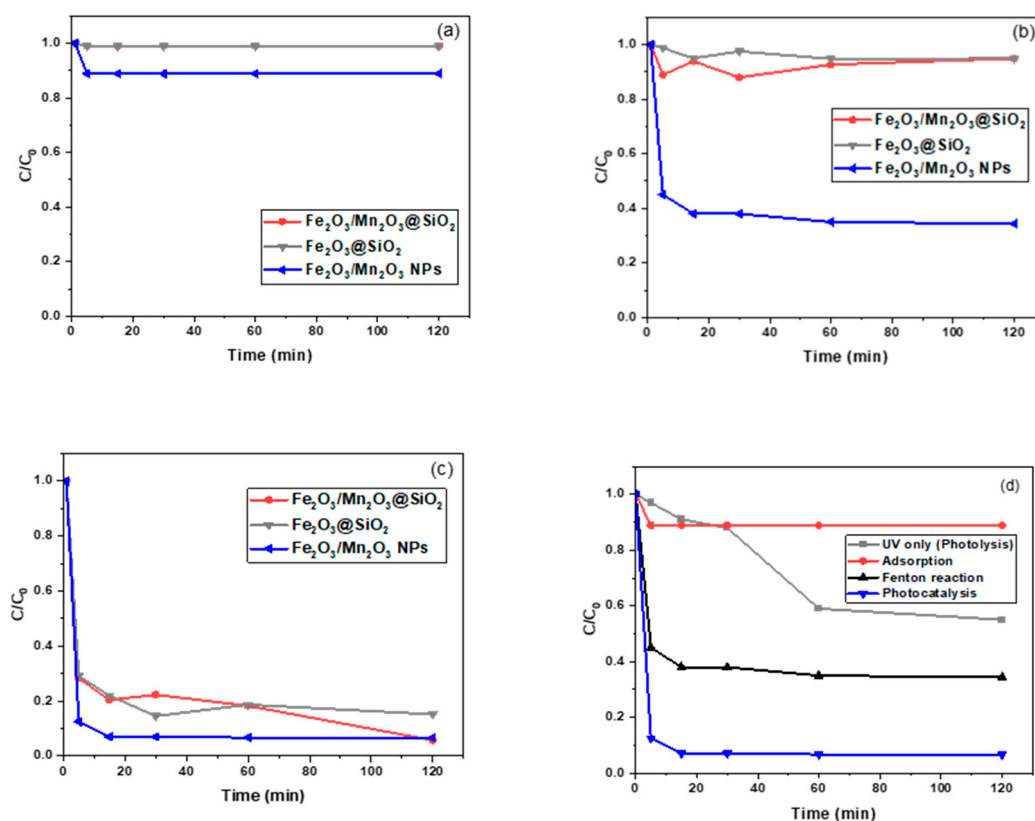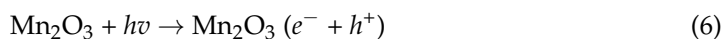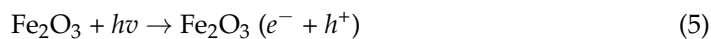
Figure 9. Degradation of Congo red (CR) with Fe_2O_3/Mn_2O_3 nanoparticles (FM-NPs), $Fe_2O_3/Mn_2O_3@SiO_2$ (FMS) under different conditions; (**a**) Only adsorption (without UV + H_2O_2), (**b**) Fenton reaction with H_2O_2 (without UV), and (**c**) Photo-Fenton reaction with UV + H_2O_2 (reaction conditions: catalyst dose = 1 g/L, initial concentration of CR = 10 mg/L, initial pH = 7), and (**d**) comparison of degradation performance with FM-NPs under different reaction conditions.

2.2.3. Possible Degradation Mechanism of Photocatalytic Adsorbent

As mentioned in previous results, the dye degradation mechanism of photocatalytic adsorbents is complicated because the removal process may be coupled with adsorption, Fenton reaction, and photocatalytic reaction. UV light can activate Fe and Mn contents in the FMS for the photocatalytic reaction and separate electron-hole pairs (Equations (5) and (6)). Subsequently, the separated electrons in the conduction band (CB) might directly reduce H_2O_2 and O_2 at the surface of the FMS, while the hole derives oxidation on the surface hydroxyl or adsorbed water to produce hydroxyl radicals (Equations (7) and (8)). This consecutive release of reactive oxygen species can effectively degrade the dye molecules in the liquid phase.

$$Fe_2O_3 + hv \rightarrow Fe_2O_3 \ (e^- + h^+) \tag{5}$$

$$Mn_2O_3 + hv \rightarrow Mn_2O_3 \ (e^- + h^+) \tag{6}$$

$$e^- + H_2O_2 \rightarrow OH + OH^- \tag{7}$$

$$h^+ + H_2O_2 \rightarrow OH + H^+ \tag{8}$$

In the case of FMS, rapid decolonization can occur through the subsequent electron transfer of the Fe_2O_3/Mn_2O_3 nanocomposite on the surface of the catalyst. The XRD pattern confirmed that the Fe_2O_3/Mn_2O_3 nanocomposites consisted of α-Fe_2O_3 and α-Mn_2O_3. As shown in the schematic diagram of the photocatalytic degradation (Figure 10), the behavior of the Fe_2O_3/Mn_2O_3 nanocomposites can be explained as type-I (straddling gap) heterojunction photocatalysis, given that the CB and valence band (VB) of Mn_2O_3 are in between those of Fe_2O_3 [44]. The bandgap energy was calculated for NPs using

UV–visible optical spectroscopy and it was found to be 1.9 eV for α-Fe$_2$O$_3$ and 1.3 eV for α-Mn$_2$O$_3$ in the literature [5,45]. Because the band edge of α-Fe$_2$O$_3$ exists above α-Mn$_2$O$_3$, photogenerated holes at the low-energy level would quickly move to the VB of α-Mn$_2$O$_3$, and high-energy electrons are transferred to the CB of α-Fe$_2$O$_3$ [46–48]. This can lead to prolonged catalytic separation and improved catalyst lifetime by hindering the recombination of electron-hole pairs. The excited electrons or holes react with molecular oxygen on the surface of the FM-NPs, and dyes can be decomposed by OH radicals and converted into CO$_2$, and H$_2$O.

Meanwhile, physical and chemical adsorption could contribute to the enhanced adsorption of cationic organic pollutants onto FMS. From previous results, SiO$_2$ in FMS can chain a hydrogel network (Si-O-Si), which has hydrophilic properties. Given that the surface charge of RhB is highly negative, colloidal interactions between the silica hydrogel and the dye can hold strong van der Waals interactions. Thus, a previous study stated that high-energy electrons potentially transfer from excited nanoparticles to the empty state of the nearby SiO$_2$ [34]. Under light sources, electron transfer occurring between the SiO$_2$ and bi-metal impregnates the surface of SiO$_2$. Another possibility is the formation of hydrogen bonding forces between the FMS and cationic dye molecules, as stated above. The possible interactions of FMS are shown in Figure 10, which shows the behavior of RhB dye adsorption onto FMS. FTIR analysis showed hydrogen-bonding donors and acceptors on the FMS surface, and the RhB molecule had hydrogen-bonding groups.
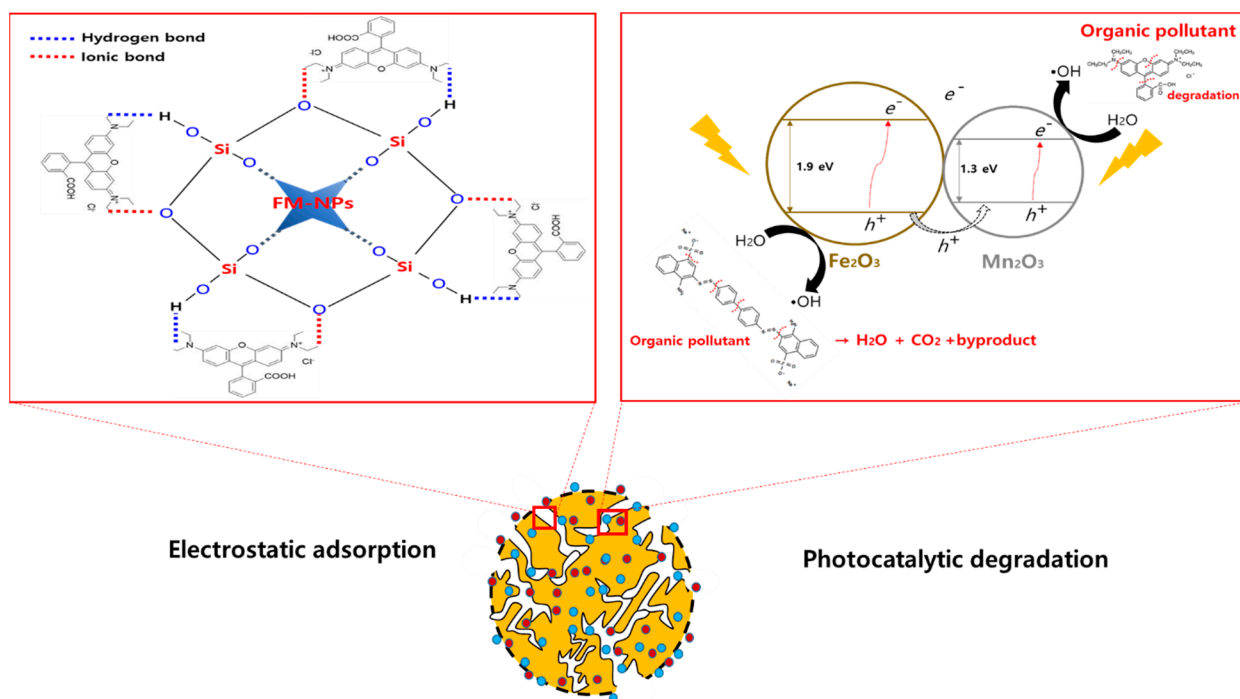

Figure 10. Schematic diagram of the degradation process of the RhB dye by the photocatalytic reaction of FMS.

3. Materials and Methods

3.1. Chemicals

Mn(NO$_3$)$_2$·4H$_2$O (>98%) and Cetyltrimethylammonium chloride (CTAC) solution (25 wt.%) were purchased from Sigma-Aldrich (MO, USA). Fe(NO$_3$)$_3$·9H$_2$O and 95% of Tetraethyl orthosilicate (TEOS) were supplied by Samchun Pure Chemicals (Pyeongtaek-si, Korea). H$_2$O$_2$ (28%) solution and NaOH (1N) were supplied by Daejung Chemicals (Seoul, Korea).

3.2. Synthesis of Catalyst-Doped Adsorbents

Fe_2O_3/Mn_2O_3: Fe_2O_3 and Mn_2O_3 were synthesized using a sonication-assisted co-precipitation method. First, 16.16 g of $Fe(NO_3)_3.9H_2O$ and 5.0 g and $Mn(NO_3)_2.4H_2O$ as precursors were dissolved in 600 mL of DI water and warmed up to 65 °C for 30 min. Then, 1 g of surfactant cetyltrimethylammonium bromide (CTAB) was added to the above solution and mixed for 120 min at 60 °C, before 2.0 mol L^{-1} of NaOH solution was added as a precipitation agent under sonication until a pH 12 was achieved. The precipitate sample was washed with DI water, dehydrated at 100 °C for 24 h, and calcined at 700 °C for 7 h.

Fe_2O_3/Mn_2O_3 @SiO_2: The obtained nanoparticles were homogenized (PREMIX Model 2.5) with 6000 rpm for 8 h. Next, 0.4 g of Fe_2O_3/Mn_2O_3 nanoparticles (FM-NPs) were mixed with 40 mL of CTAC for 30 min at 40 °C, and 40 mL of TEOS was added to the mixture and converted to a black colored gel immediately. The obtained gel was incubated for 24 h at 50 °C under 200 rpm stirrer, then calcinated in a furnace at an increasing rate of 2 °C/min until 550 °C, which was continued for 6 h.

3.3. Characterization

The surface characterization of synthesized photocatalytic adsorbent was analyzed using scanning electron microscopy (SEM) (JEOL-7800F, Tokyo, Japan). Hence, 2D elemental mapping was analyzed by using energy-dispersive X-ray spectroscopy (EDS). Transmission electron microscopy (TEM) images were analyzed using a Philips CM200 (Amsterdam, The Netherlands), and EDS DX-4 (EDAX) was used for element mapping. N_2 adsorption–desorption isotherms were measured for Brunauer–Emmett–Teller (BET) analysis to investigate porosity properties and specific surface area of synthesized materials, using a Gemini series Micromeritics 2360 instrument (Norcross, GA, USA). The X-ray diffraction pattern was analyzed to investigate the composition and phase structure of the synthesized material composites using a Rigaku D/Max-2500 X-ray (Tokyo, Japan) diffractometer, and FTIR spectra (Vertex 70, Bruker, MA, USA) of the samples were analyzed to measure the vibrations and rotations of molecular functional groups. Electron spin resonance (ESR) spectrometer was applied to analyze oxidation state of metal complexes using a JEOL JES-FE1C X-band spectrometer (Tokyo, Japan). X-ray photoelectron spectroscopy (XPS) analysis was carried out to investigate the elemental oxidation state of synthesized material (K-alpha, London, Thermo UK) and deconvoluted with Fityk software. UV–Vis spectroscopy (LAMBDA 365 UV–Vis Spectro-photometer, Perkin Elmer, MA, USA) measured the sample solution to detect dye concentration before and after treatment.

3.4. Dye Degradation Procedure

The performance of FMS as a photocatalytic adsorbent was tested for the removal of cationic and anionic dyes under different reaction conditions including adsorption, the Fenton reaction, and photocatalysis. Rhodamine B (RhB, >95%, Sigma-Aldrich, MO, USA) and Congo red (CR, >97%, Sigma-Aldrich, MO, USA) were selected as the cationic and anionic dye removal indicators, respectively, for the photocatalytic experiment. For the photocatalytic test, an acryl reactor with UV lamps (8 W, 254 nm, Philips, The Netherlands) was fitted, and 100 mg of photocatalytic adsorbent and 100 mL of dye solution with a concentration of 10 mg/L were injected into a quartz cell tube. Different experimental conditions, such as adsorption without UV, H_2O_2 addition without UV (Fenton), and H_2O_2 addition under UV (photocatalytic reaction), were operated at 22 ± 2 °C and pH around 7. Samples were collected at 0, 5, 15, 30, 60, and 120 min using a syringe filter (0.45 μm) to separate the photocatalytic adsorbent and they were analyzed using UV–Vis spectroscopy to measure the dye concentration before and after the reaction by the following Equation (9)

$$Dye\ removal\ efficiency\ (\%) = (\frac{C_0 - C_t}{C_0}) \times 100 \qquad (9)$$

where C_0 is the initial concentration of dye solution and C_t is the final concentration of dye at a reaction time. All dye degradation experiments were performed in a duplicate, and the results represent an average value.

4. Conclusions

Results indicate that the degradation of dyes is a photocatalytic adsorption-driven process, and the charge properties of the target pollutants are important. RhB, a representative cationic molecule, showed excellent reduction by adsorption with FMS, and the reduction efficiency was greatly increased in the presence of H_2O_2 and UV, mainly because the adsorption by the negatively charged silica supports the mitigation of electron-hole recombination from the photocatalyst. This is also revealed through the CR adsorption experiment, which is an anionic molecule, and it was found that the reduction efficiency was significantly lower than that of RhB owing to the electro-repulsion effect between the silica surface and CR. However, in this case, it was found that the reduction by the bimetallic FM-NPs catalyst was effective under the photocatalytic process. The generation of the reactive oxygen species can be attributed to the creation of photo-induced charge carriers by bi-metal NPs and their interactions with oxygen and water molecules on the surface of the particles. A synergistic effect of the additional impregnation of SiO_2 on the FM-NPs was observed, leading to photocatalytic adsorption.

References

1. Smol, M.; Włodarczyk-Makuła, M. The effectiveness in the removal of PAHs from aqueous solutions in physical and chemical processes: A review. *Polycycl. Aromat. Compd.* **2017**, *37*, 292–313. [CrossRef]
2. Gerba, C.P.; Betancourt, W.Q.; Kitajima, M.; Rock, C.M. Reducing uncertainty in estimating virus reduction by advanced water treatment processes. *Water Res.* **2018**, *133*, 282–288. [CrossRef] [PubMed]
3. Jeon, J.-H.; Kim, S.-H.; Lee, S.-W.; Kim, S.-O. Photocatalytic Oxidation of Arsenite Using Goethite and UV LED. *J. Korean Soc. Environ. Eng.* **2017**, *39*, 9–18. [CrossRef]
4. Kumar, N.; Yadav, S.; Mittal, A.; Kumari, K. Photocatalysis by zinc oxide-based nanomaterials. In *Nanostructured Zinc Oxide*; Elsevier: Amsterdam, The Netherlands, 2021; pp. 393–457.
5. Gupta, N.K.; Ghaffari, Y.; Bae, J.; Kim, K.S. Synthesis of coral-like α-Fe_2O_3 nanoparticles for dye degradation at neutral pH. *J. Mol. Liq.* **2020**, *301*, 112473. [CrossRef]
6. Zhao, Y.; Deng, N.; Fan, Z.; Hu, Z.-T.; Fan, L.; Zhou, J.; Huang, X. On-site H_2O_2 electro-generation process combined with ultraviolet: A promising approach for odorous compounds purification in drinking water system. *Chem. Eng. J.* **2022**, *430*, 132829. [CrossRef]
7. Ghaffari, Y.; Gupta, N.K.; Bae, J.; Kim, K.S. One-step fabrication of Fe_2O_3/Mn_2O_3 nanocomposite for rapid photodegradation of organic dyes at neutral pH. *J. Mol. Liq.* **2020**, *315*, 113691. [CrossRef]
8. Arzate, S.; Pfister, S.; Oberschelp, C.; Sánchez-Pérez, J.A. Environmental impacts of an advanced oxidation process as tertiary treatment in a wastewater treatment plant. *Sci. Total Environ.* **2019**, *694*, 133572. [CrossRef]
9. Rui, J.; Deng, N.; Zhao, Y.; Tao, C.; Zhou, J.; Zhao, Z.; Huang, X. Activation of persulfate via Mn doped Mg/Al layered double hydroxide for effective degradation of organics: Insights from chemical and structural variability of catalyst. *Chemosphere* **2022**, *302*, 134849. [CrossRef]
10. Kharisov, B.I.; Kharissova, O.V.; Rasika Dias, H.; Ortiz Méndez, U.; Gómez De La Fuente, I.; Peña, Y.; Vázquez Dimas, A. *Iron-based Nanomaterials in the Catalysis*; InTech: Rijeka, Croatia, 2016.
11. Wang, G.; Tang, K.; Jiang, Y.; Andersen, H.R.; Zhang, Y. Regeneration of Fe (II) from Fenton-derived ferric sludge using a novel biocathode. *Bioresour. Technol.* **2020**, *318*, 124195. [CrossRef]
12. Lam, F.L.; Hu, X. pH-insensitive bimetallic catalyst for the abatement of dye pollutants by photo-fenton oxidation. *Ind. Eng. Chem. Res.* **2013**, *52*, 6639–6646. [CrossRef]
13. Xu, M.; Wu, C.; Zhou, Y. Advancements in the Fenton process for wastewater treatment. *Adv. Oxid. Process* **2020**, *61*, 61–77.

14. Baek, S.; Joo, S.H.; Su, C.; Toborek, M. Antibacterial effects of graphene-and carbon-nanotube-based nanohybrids on Escherichia coli: Implications for treating multidrug-resistant bacteria. *J. Environ. Manag.* **2019**, *247*, 214–223. [CrossRef] [PubMed]

15. Ghasemi, H.; Mozaffari, S.; Mousavi, S.H.; Aghabarari, B.; Abu-Zahra, N. Decolorization of wastewater by heterogeneous Fenton reaction using MnO_2-Fe_3O_4/CuO hybrid catalysts. *J. Environ. Chem. Eng.* **2021**, *9*, 105091. [CrossRef]

16. Li, Z.; Tang, X.; Liu, K.; Huang, J.; Xu, Y.; Peng, Q.; Ao, M. Synthesis of a MnO_2/Fe_3O_4/diatomite nanocomposite as an efficient heterogeneous Fenton-like catalyst for methylene blue degradation. *Beilstein J. Nanotechnol.* **2018**, *9*, 1940–1950. [CrossRef]

17. Ajiboye, T.O.; Oyewo, O.A.; Onwudiwe, D.C. Adsorption and photocatalytic removal of Rhodamine B from wastewater using carbon-based materials. *FlatChem* **2021**, *29*, 100277. [CrossRef]

18. Alshorifi, F.T.; Tobbala, D.E.; El-Bahy, S.M.; Nassan, M.A.; Salama, R.S. The role of phosphotungstic acid in enhancing the catalytic performance of UiO-66 (Zr) and its applications as an efficient solid acid catalyst for coumarins and dihydropyrimidinones synthesis. *Catal. Commun.* **2022**, *169*, 106479. [CrossRef]

19. Yahya, N.; Aziz, F.; Jamaludin, N.; Mutalib, M.; Ismail, A.; Salleh, W.; Jaafar, J.; Yusof, N.; Ludin, N. A review of integrated photocatalyst adsorbents for wastewater treatment. *J. Environ. Chem. Eng.* **2018**, *6*, 7411–7425. [CrossRef]

20. Gupta, N.K.; Bae, J.; Baek, S.; Kim, K.S. Metal-organic framework-derived NaMxOy adsorbents for low-temperature SO_2 removal. *Chemosphere* **2022**, *291*, 132836. [CrossRef]

21. Yu, L.; Liu, H.; Liu, C.; Lan, H.; Qu, J. Magnetically-Confined Fe-Mn Bimetallic Oxide Encapsulation as an Efficient and Recoverable Adsorbent for Arsenic (III) Removal. *Part. Part. Syst. Charact.* **2016**, *33*, 323–331. [CrossRef]

22. Fanourakis, S.K.; Peña-Bahamonde, J.; Bandara, P.C.; Rodrigues, D.F. Nano-based adsorbent and photocatalyst use for pharmaceutical contaminant removal during indirect potable water reuse. *NPJ Clean Water* **2020**, *3*, 1. [CrossRef]

23. Kamegawa, T.; Yamahana, D.; Yamashita, H. Graphene coating of TiO_2 nanoparticles loaded on mesoporous silica for enhancement of photocatalytic activity. *J. Phys. Chem. C* **2010**, *114*, 15049–15053. [CrossRef]

24. Bilgic, A. Fabrication of monoBODIPY-functionalized Fe_3O_4@ SiO_2@ TiO_2 nanoparticles for the photocatalytic degradation of rhodamine B under UV irradiation and the detection and removal of Cu (II) ions in aqueous solutions. *J. Alloys Compd.* **2022**, *899*, 163360. [CrossRef]

25. Do, Q.C.; Kim, D.-G.; Ko, S.-O. Catalytic activity enhancement of a Fe_3O_4@ SiO_2 yolk-shell structure for oxidative degradation of acetaminophen by decoration with copper. *J. Clean. Prod.* **2018**, *172*, 1243–1253. [CrossRef]

26. ALOthman, Z.A. A review: Fundamental aspects of silicate mesoporous materials. *Materials* **2012**, *5*, 2874–2902. [CrossRef]

27. Ghaffari, Y.; Gupta, N.K.; Bae, J.; Kim, K.S. Heterogeneous catalytic performance and stability of iron-loaded ZSM-5, zeolite-A, and silica for phenol degradation: A microscopic and spectroscopic approach. *Catalysts* **2019**, *9*, 859. [CrossRef]

28. Kim, S.; Gupta, N.K.; Bae, J.; Kim, K.S. Structural variations and generation of binding sites in Fe-loaded ZSM-5 and silica under the effect of UV-irradiation and their role in enhanced BTEX abatement from gas streams. *J. Hazard. Mater.* **2020**, *384*, 121274. [CrossRef]

29. Kumar, G.H.; Rao, J.L.; Gopal, N.; Narasimhulu, K.; Chakradhar, R.; Rajulu, A.V. Spectroscopic investigations of Mn^{2+} ions doped polyvinylalcohol films. *Polymer* **2004**, *45*, 5407–5415. [CrossRef]

30. Kim, S.; Gupta, N.K.; Bae, J.; Kim, K.S. Fabrication of coral-like Mn_2O_3/Fe_2O_3 nanocomposite for room temperature removal of hydrogen sulfide. *J. Environ. Chem. Eng.* **2021**, *9*, 105216. [CrossRef]

31. Slatineanu, T.; Diana, E.; Nica, V.; Oancea, V.; Caltun, O.; Iordan, A.; Palamaru, M. The influence of the chelating/combustion agents on the structure and magnetic properties of zinc ferrite. *Open Chem.* **2012**, *10*, 1799–1807. [CrossRef]

32. Roosendaal, S.; Van Asselen, B.; Elsenaar, J.; Vredenberg, A.; Habraken, F. The oxidation state of Fe (100) after initial oxidation in O_2. *Surf. Sci.* **1999**, *442*, 329–337. [CrossRef]

33. Carley, A.; Jackson, S.; O'shea, J.; Roberts, M. The formation and characterisation of Ni^{3+}—An X-ray photoelectron spectroscopic investigation of potassium-doped Ni (110)–O. *Surf. Sci.* **1999**, *440*, L868–L874. [CrossRef]

34. Ghaffari, Y.; Beak, S.; Bae, J.; Saifuddin, M.; Kim, K.S. Effect of UV Irradiation on the Structural Variation of Metal Oxide-Silica Nanocomposites for Enhanced Removal of Erythromycin at Neutral pH. *Catalysts* **2022**, *12*, 424. [CrossRef]

35. Park, Y.; Woo Lee, S.; Kim, K.H.; Min, B.-K.; Kumar Nayak, A.; Pradhan, D.; Sohn, Y. Understanding hydrothermal transformation from Mn_2O_3 particles to $Na_{0.55}Mn_2O_4$ 1.5 H_2O nanosheets, nanobelts and single crystalline ultra-long $Na_4Mn_9O_{18}$ nanowires. *Sci. Rep.* **2015**, *5*, 18275. [CrossRef] [PubMed]

36. Sarmah, K.; Pratihar, S. Synthesis, characterization, and photocatalytic application of iron oxalate capped Fe, Fe–Cu, Fe–Co, and Fe–Mn oxide nanomaterial. *ACS Sustain. Chem. Eng.* **2017**, *5*, 310–324. [CrossRef]

37. Huang, H.; Cao, R.; Yu, S.; Xu, K.; Hao, W.; Wang, Y.; Dong, F.; Zhang, T.; Zhang, Y. Single-unit-cell layer established Bi_2WO_6 3D hierarchical architectures: Efficient adsorption, photocatalysis and dye-sensitized photoelectrochemical performance. *Appl. Catal. B Environ.* **2017**, *219*, 526–537. [CrossRef]

38. Espinosa, J.C.; Catalá, C.; Navalon, S.; Ferrer, B.; Álvaro, M.; Garcia, H. Iron oxide nanoparticles supported on diamond nanoparticles as efficient and stable catalyst for the visible light assisted Fenton reaction. *Appl. Catal. B Environ.* **2018**, *226*, 242–251. [CrossRef]

39. Dang, X.; Zhao, H. Bimetallic Fe/Mn metal-organic-frameworks and Au nanoparticles anchored carbon nanotubes as a peroxidase-like detection platform with increased active sites and enhanced electron transfer. *Talanta* **2020**, *210*, 120678. [CrossRef]

40. Eslami, H.; Ehrampoush, M.H.; Esmaeili, A.; Ebrahimi, A.A.; Ghaneian, M.T.; Falahzadeh, H.; Salmani, M.H. Synthesis of mesoporous Fe-Mn bimetal oxide nanocomposite by aeration co-precipitation method: Physicochemical, structural, and optical properties. *Mater. Chem. Phys.* **2019**, *224*, 65–72. [CrossRef]

41. Saini, J.; Garg, V.; Gupta, R. Removal of methylene blue from aqueous solution by $Fe_3O_4@ Ag/SiO_2$ nanospheres: Synthesis, characterization and adsorption performance. *J. Mol. Liq.* **2018**, *250*, 413–422. [CrossRef]

42. Anisuzzaman, S.; Joseph, C.G.; Pang, C.K.; Affandi, N.A.; Maruja, S.N.; Vijayan, V. Current Trends in the Utilization of Photolysis and Photocatalysis Treatment Processes for the Remediation of Dye Wastewater: A Short Review. *ChemEngineering* **2022**, *6*, 58. [CrossRef]

43. Yimin, D.; Jiaqi, Z.; Danyang, L.; Lanli, N.; Liling, Z.; Yi, Z.; Xiaohong, Z. Preparation of Congo red functionalized $Fe_3O_4@ SiO_2$ nanoparticle and its application for the removal of methylene blue. *Colloids Surf. A Physicochem. Eng. Asp.* **2018**, *550*, 90–98. [CrossRef]

44. Sharrouf, M.; Awad, R.; Marhaba, S.; El-Said Bakeer, D. Structural, optical and room temperature magnetic study of Mn-doped ZnO nanoparticles. *Nano* **2016**, *11*, 1650042. [CrossRef]

45. Ghosh, S.K. Diversity in the family of manganese oxides at the nanoscale: From fundamentals to applications. *ACS Omega* **2020**, *5*, 25493–25504. [CrossRef]

46. Ahamed, I.; Seriani, N.; Gebauer, R.; Kashyap, A. Heterostructures of ε-Fe_2O_3 and α-Fe_2O_3: Insights from density functional theory. *RSC Adv.* **2020**, *10*, 27474–27480. [CrossRef]

47. Kurien, U.; Hu, Z.; Lee, H.; Dastoor, A.P.; Ariya, P.A. Radiation enhanced uptake of Hg 0 (g) on iron (oxyhydr) oxide nanoparticles. *RSC Adv.* **2017**, *7*, 45010–45021. [CrossRef]

48. Luan, P.; Xie, M.; Liu, D.; Fu, X.; Jing, L. Effective charge separation in the rutile TiO_2 nanorod-coupled α-Fe_2O_3 with exceptionally high visible activities. *Sci. Rep.* **2014**, *4*, 6180. [CrossRef] [PubMed]